Columnar growth and surface chemistry of NiFeCrCo high entropy alloy thin films by magnetron sputtering

Running title: NiFeCrCo high entropy alloy thin films by magnetron sputtering

Running Authors: Hongfei Liu

Yee Ng[1], Jingcong Hu[2], Debbie H.L. Seng[1], Anna Marie Yong[1], Ming Lin[1], and Hongfei Liu[1, a)]

[1]Institute of Materials Research and Engineering (IMRE), A*STAR (Agency for Science, Technology and Research), 2 Fusionopolis Way, Singapore 138634, Singapore

[2]Department of Chemical and Biomolecular Engineering, National University of Singapore, 4 Engineering Drive 4, Singapore 117585, Singapore.

[a)] Electronic mail: liuhf@a-star.edu.sg

Scanning electron microscopy, transmission electron microscopy, energy dispersive X-ray (EDX) spectroscopy, and X-ray photoelectron (XPS) spectroscopy were used to study the microstructure and surface chemistry of NiFeCrCo-on-Si(001) thin films grown by magnetron sputtering at 100 °C using near-equiatomic NiFeCrCo target. It was revealed that the high entropy alloy (HEA) thin films predominantly exhibits [111]-oriented face-centered cubic (FCC) submicron columns. The diameter of the columnar grains increased progressively along the growth direction. Two types of grain boundaries were identified. One type formed between adjacent columnar grains, while the other originated within individual columns, consisting of nanotwinnings and stacking faults inclined to the columnar growth direction. Their densities increased in the regions near the film surface. XPS and EDX indicated a surface oxidation tendency of Cr > Fe ~ Co > Ni, despite compositional variations (< ±2.0 at.%) induced by varied sputtering power, which correlated well with the segregation-induced surficial elemental distributions. These

findings provide new insights into the growth behavior of HEA thin films produced by magnetron sputtering.

I. INTRODUCTION

High-entropy alloys (HEAs) have emerged as a transformative class of materials distinguished by their near-equiatomic multicomponent compositions, resulting in sluggish diffusion, lattice distortion, compositional complexity, and thus leading to the enhancement of mechanical and radiation tolerance.[1] This unique alloying strategy stabilizes simple solid-solution phases, typically face-centered cubic (FCC), body-centered cubic (BCC), or mixed structures, over complex intermetallic compounds.[2-3] HEAs combine structural simplicity with remarkable combinations of properties which includes high strength, high-temperature stability, corrosion resistance, irradiation tolerance, and wear resistance.[4-5] These attributes have spurred growing interest in the development HEA thin films, where the intrinsic advantages of HEAs can be further tailored through microstructural control, size effects, and non-equilibrium processes during film deposition.[6-9] HEA thin films fabricated by physical vapor deposition techniques such as magnetron sputtering, pulsed laser deposition, and cathodic arc evaporation often display supersaturated solid solutions, refined grain structures, and controllable textures.[10-13] Their deposition-driven non-equilibrium nature enables extended solubility ranges and metastable microstructures not achievable in bulk forms, offering pathways to tune mechanical, electrical, and chemical behavior for functional applications.[14-15] Consequently, HEA thin films have found increasing relevance in protective coatings, microelectromechanical systems (MEMS), diffusion barriers, and high-temperature or corrosive environments.[16-19]

Among the various HEA families, NiFeCrCo-based HEAs have garnered attention due to their stable single-phase FCC structure, good mechanical performance, and excellent chemical and thermal stability.[20-21] The well-studied NiFeCrCo system has been recognized as a model HEA due to its simple crystal structure and well-characterized deformation behavior. When synthesized as thin films, NiFeCrCo-based HEAs exhibit tunable columnar or nanocrystalline microstructures depending on the deposition conditions such as power, working pressure, substrate temperature, and bias.[21-25] The relatively low stacking fault energy (SFE) of NiFeCrCo-based HEA enables nanotwinnings, stacking faults, and extensive defect interactions.[26] These microstructural variations significantly affect hardness, ductility, residual stress, and oxidation or corrosion resistance.[27] Moreover, the reduced dimensionality and rapid adatom kinetics allow the stabilization of metastable configurations, altered elemental distributions, and enhanced lattice strain, providing deeper insight into fundamental HEA mechanisms, e.g., lattice distortion, sluggish diffusion, and solid-solution strengthening.

The combination of inherent HEA attributes and thin-film deposition effects makes NiFeCrCo-based HEA thin films a promising advanced engineering solution which include wear-resistant coatings, diffusion-resistant barriers, and corrosion-protective surfaces. At the same time, their relatively simple quaternary chemistry makes them an ideal platform for exploring the relationships among deposition condition, microstructural evolution, and resulting properties. Understanding the growth behavior, particularly columnar grain formation, and the accompanying structural features, including the nanotwinnings and stacking faults, is therefore pivotal for both practical optimization and fundamental materials science.

II. EXPERIMENTAL

NiFeCrCo thin films were deposition on Si(001) substrates at 100 °C by magnetron sputtering using a near-equiatomic 4-inch diameter NiFeCrCo target.[25] The magnetron sputtering system, with a background pressure higher than 4×10^{-7} Torr, was initially designed for the growth of semiconductor thin films with high thickness uniformities across 200-mm-diameter wafers.[28-30] Pure argon (99.95 %) was used as the working gas, maintained at 5.0×10^{-3} Torr by a pumping system, along with a throttle valve and an argon flow rate of 5.0 SCCM. A calibration of the thin film growth rate under these conditions for 120 min revealed a linear increase from ~0.7 to ~7.1 nm/min by increasing the radio-frequency (RF) power applied on the NiFeCrCo target from 50 to 300 W.[25]

The microstructure properties of the NiFeCrCo HEA thin films were investigated by scanning electron microscopy (JSM-FESEM 7600F) and transmission electron microscopy (TEM). Energy dispersive X-ray spectroscopy (EDX), in both the SEM and TEM chambers, and X-ray photoelectron spectroscopy (XPS) were applied to examine the surface chemistry of the NiFeCrCo HEA thin films. For the EDX in the SEM chamber, the electron beam was accelerated at 15.0 kV, resulting in a probe current of ~6.0 A. Cross-sectional TEM lamellae were prepared using a dual-beam focused ion beam/scanning electron microscopy (FIB-SEM) system (FEI Helios NanoLab 450S). Prior to milling, a protective Pt capping layer was deposited on the film surface, consisting of a 0.5-μm-thick electron-beam deposition followed by a 2-μm-thick ion-beam deposition, to avoid ion-induced damage during trenching. Standard lift-out

procedures were performed using a 30 kV Ga^+ ion beam with currents of 0.1~21 nA for coarse milling and thinning. Final polishing of the lamellae was conducted at 2.0 kV with a 23 pA Ga^+ beam to minimize surface amorphization and preserve intrinsic microstructures. High-resolution TEM (HRTEM) and high-angle annular dark-field (HAADF) scanning TEM (STEM) measurements were carried out on a Spectra-300 (Thermo Fisher Scientific) aberration-correct TEM system operated at 200 kV. The spherical-aberration (Cs) corrector enabled sub-angstrom spatial resolution for direct imaging of lattice fringes and atomic-scale microstructural features. The imaging was performed using a convergence semi-angle of ~21.3 mrad. Elemental mapping was conducted using the Super-EDS system in the TEM chamber, equipped with dual windowless silicon drift detectors for high-sensitivity EDX. XPS was carried out in an Axis-Supra-Plus-XPS system with Al-Kα (hν = 1486.7 eV). The spot size was focused to 700 μm × 300 μm and the scanning step was 0.1 eV for probing the core levels.

III. RESULTS AND DISCUSSION

SEM images taken from the surface of the obtained NiFeCrCo-on-Si thin films exhibit absence of any surface features when the RF power is lower than 150 W. However, roughened surface emerged at 150 W and the surface features grown larger with the increase in the RF power to 300 W.[25] Typical SEM images taken from the surfaces of the thin films grown at 150 and 300 W are shown in Figs. 1(a) and 1(b), respectively. Likewise, those from the cross sections are presented in Figs. 1(c) and 1(d), respectively. They show the typical columnar growth with increased column diameter at higher RF power, leading to the larger surface features. Presented in Figs. 1(e)-1(h) are

the elemental distributions of Ni, Fe, Cr, and Co, respectively, which were taken by EDX from the same surface areas as shown in Fig. 1(b), exhibiting absence of segregations.

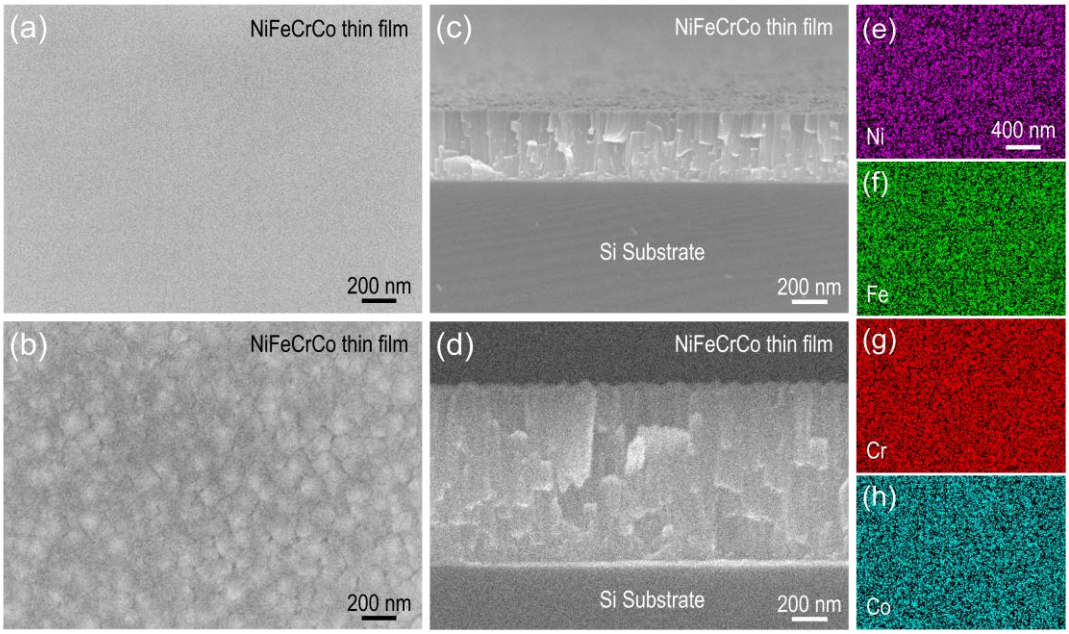

FIG. 1. SEM/EDX images. Top-view (a)-(b) and cross-sectional (c)-(d) SEM images taken from NiFeCrCo thin films grown with RF power at 150 and 300 W, respectively. (e)-(h) EDX maps from the same areas in (b) for Ni, Fe, Cr, and Co, respectively.

Figure 2 presents the cross-sectional STEM images taken in HAADF-mode from the NiFeCrCo-on-Si HEA thin films grown with the RF power at 300 W. Presented in Fig. 2(a) is a typical HAADF image, showing the overall thickness of the thin film in columnar structures with the column diameter progressively increasing along the growth direction. Figures 2(b) is a HAADF image showing abundance of defective structures along with the columnar grains. Figure 2(c) presents a HAADF image at higher magnification at the regions near the surface of the NiFeCrCo-on-Si HEA thin film, exhibiting two types of grain boundaries. Type-I formed between adjacent vertical columnar grains, as indicated by the downward arrows, while type-II originated within

individual columns, inclined to the columnar growth directions, as indicated by the upward arrows. A careful examination of Fig. 2(c) provides evidence that the intercolumnar grain boundaries are formed by adjacent seeding, growth, and merging of individual columnar grains. In comparison, the regularly inclined grain boundaries have a higher density at the region closer to the film surface. This, together with their inner-grain origination nature, indicates that the inclined grain boundaries are grain defects, through which the columnar grain releases its stress along with crystal growth.

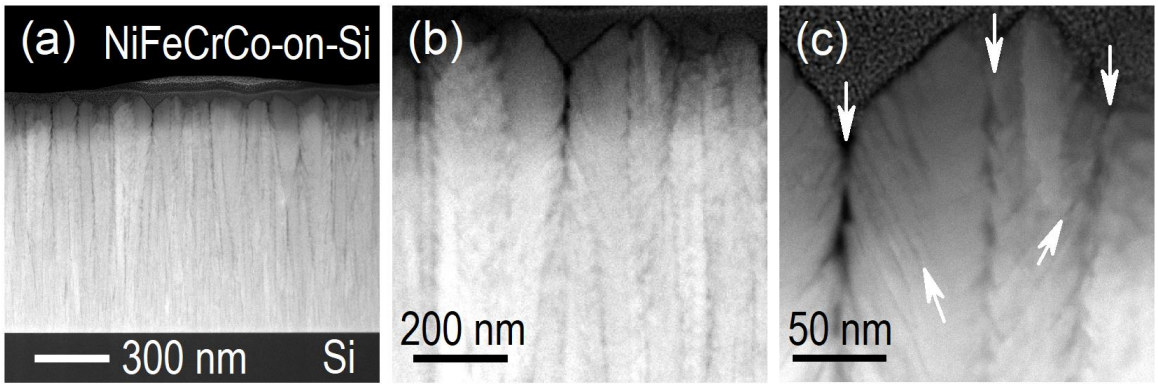

FIG. 2. Cross-sectional HAADF-STEM images taken with varied magnifications from the NiFeCrCo-on-Si HEA thin film grown with RF power at 300 W.

Figures 3(a)-3(f) present a HAADF-STEM image and its corresponding EDX mappings of O, Ni, Fe, Cr, and Co, respectively, collected from the cross-section of the NiFeCrCo-on-Si HEA thin film grown with the RF power of 300 W. Their combinations revealed that O is rich at the type-I grain boundaries, i.e., the vertically aligned ones in between adjacent columnar grains, rather than at the type-II grain boundaries, those inclined to growth direction [see Figs. 3(a) and 3(b)]. However, no oxide scales could be resolved by TEM in the O-rich regions, where all Ni, Fe, Cr, and Co are poor [see Figs. 3(c)-3(f)]. These observations indicate that the O inclusion occurred most likely after the

thin film deposition, e.g., via inward diffusion along the type-I grain boundaries in the air environment, rather than during the magnetron sputtering.

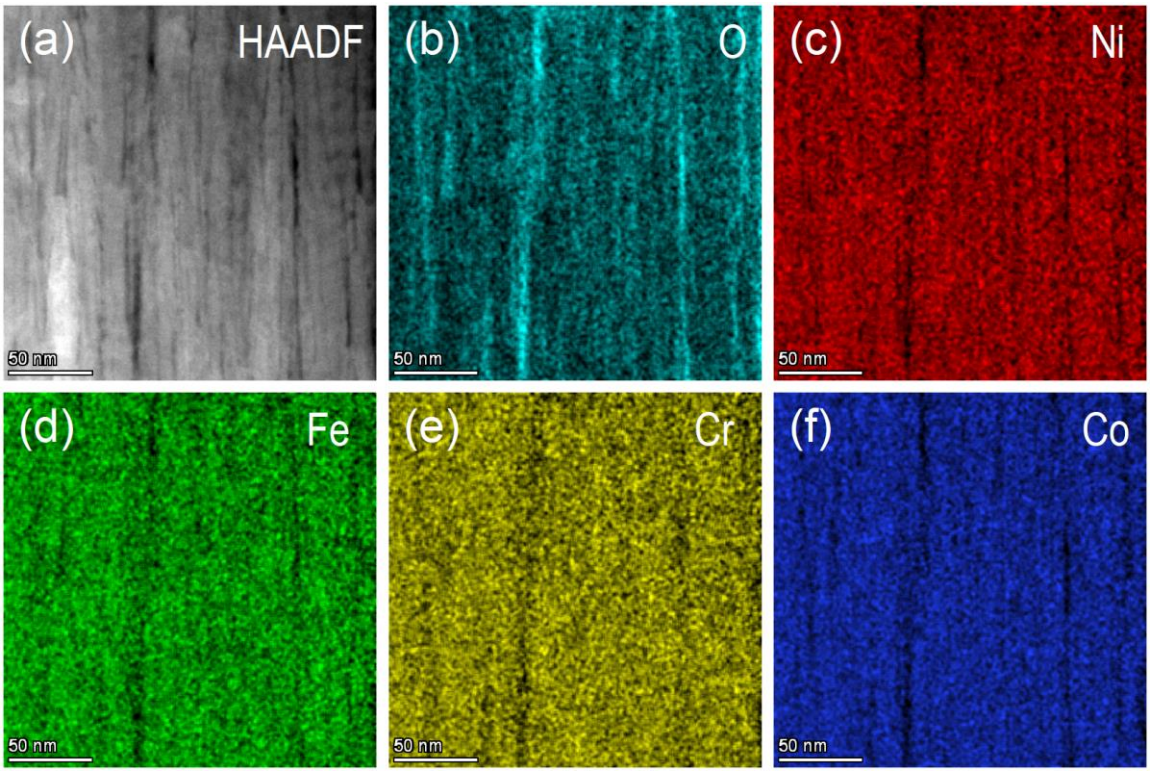

FIG. 3. Cross-sectional HAADF-STEM image (a) and its corresponding EDX maps of O, Ni, Fe, Cr, and Co in (b)-(f), respectively. The scale bar is 50 nm.

Figure 4 presents the TEM images taken in bright-field mode with varied magnifications from the NiFeCrCo-on-Si HEA thin film deposited by the magnetron sputtering with RF power at 300 W. Figures 4(a)-4(c) indeed show columnar growth of the HEA thin film with the intercolumn boundaries brighter than the column interior, as indicated by the arrows in Fig. 4(c), i.e., the grain boundaries that facilitated the inward diffusions of O. They also show inclined defects, particularly, as those seen in Figs. 4(b)-4(d), across the columnar grains, alongside fragmental vertical grain boundaries, as

indicated by the dashed lines in Fig. 4(d). It is worth mentioning that EDX mapping could not distinguish any nonuniformity of the elemental distributions within columnar grains in Fig. 4(d), indicating that the defective area, as highlighted by the dashed circle, is artificial, e.g., more pattern, rather than precipitate structures. A comparison between Figs. 4(d) and 2(c) suggests that the inclined defects across the individual columnar grains are most likely stacking faults and/or nanotwinning structures, which stack up along the column growth direction.[1, 26, 31]

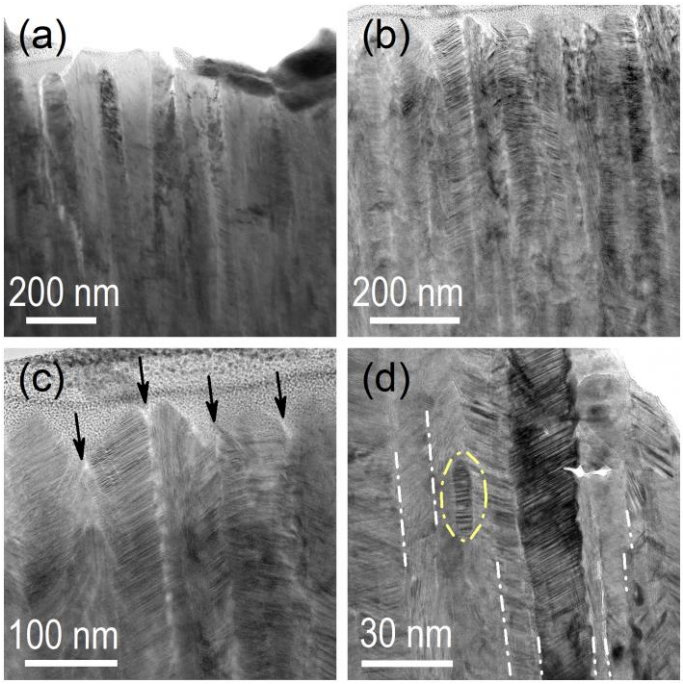

FIG. 4. Cross-sectional bright-field TEM images with varied magnifications taken from the NiFeCrCo-on-Si HEA thin film.

A typical HRTEM image of the inclined defects across the columnar grain is shown in Fig. 5(a). Presented in Figs. 5(b) and 5(c) are area-selective inverse fast Fourier transform (IFFT) images. Figure 5(c) presents the fast Fourier transform (FFT) patterns corresponding to the IFFT image in Fig. 5(b). A careful examination of the FFT patterns

in Fig. 5(d) reveals typical twin structures aligned with the twin boundary (TB)parallel to the (111) atomic planes. This is clearly seen in the IFFT image in Fig. 5(c). The lines in Fig. 5(d), linking the diffraction patterns along [111] direction, could be attributed to stacking faults (SF), as those indicated by the arrows in Fig. 5(b), near the TBs. Detailed analysis of the twin structures in Fig. 5(a) revealed an average width of ~2.0 nm, which is consistent with that reported by Chang et al.[1] in NiFeCrCo HEA thin films deposited using a pulsed direct current sputtering technique. The combination of the high entropy and the nanotwins structure was demonstrated to enhance radiation resistance, outperforming those of traditional alloys and nanocrystalline alloy thin films.[1]

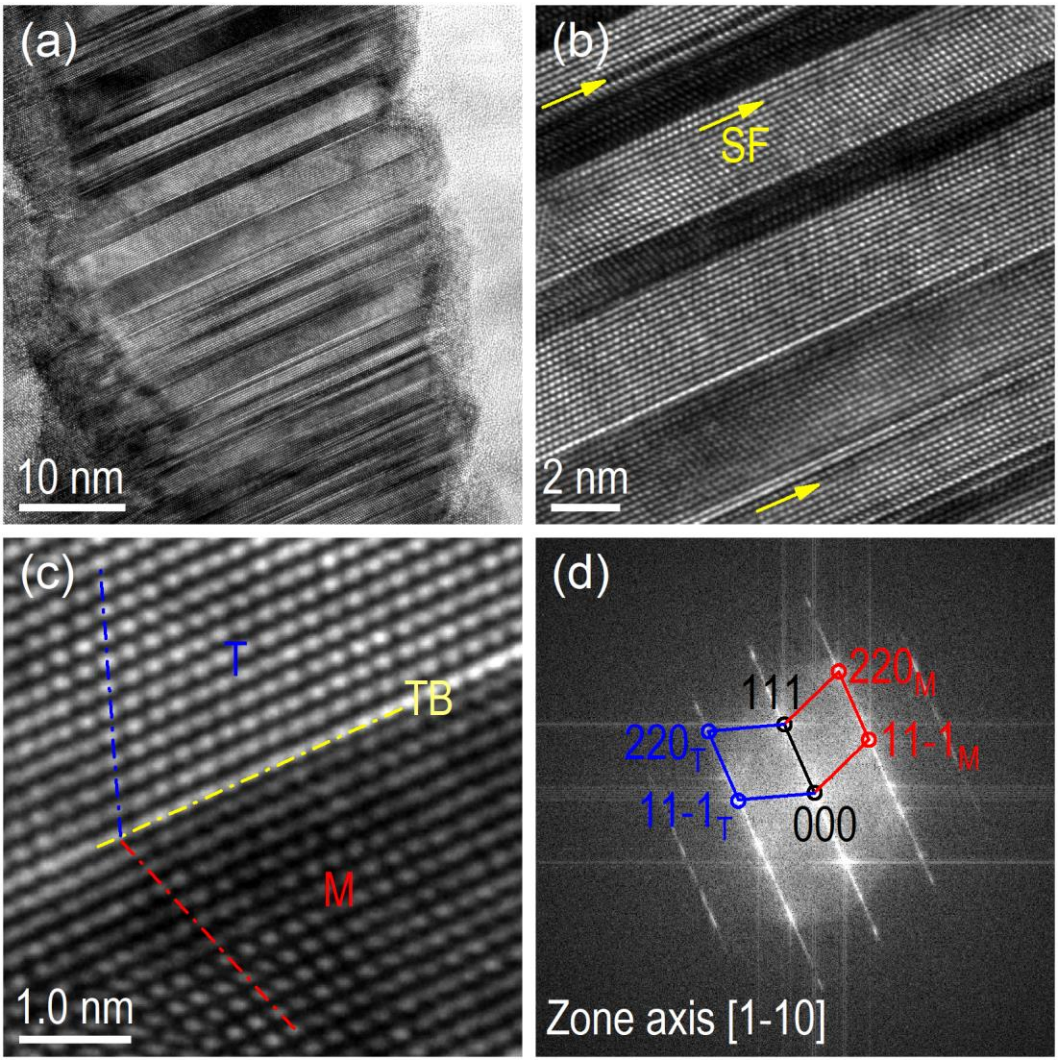

FIG. 5. Cross-sectional bright-field HRTEM image (a), selective inverse fast Fourier transform (IFFT) images (b) and (c), and fast Fourier transform (FFT) from the same area as that of the IFFT image in (b).

Figure 6 presents the core-level spectra collected by XPS from the surfaces of the NiFeCrCo HEA thin films deposited by magnetron sputtering with the RF powers ranging from 50 to 300 W. The spectra were collectively shifted by aligning the main C1s peak to 284.8 eV [see Fig. 6(a)]. Figure 6(b) shows that O is chemically absorbed on the surface of the NiFeCrCo HEA thin films with the peak intensities slightly decreased with the increase in the RF powers. Figures 6(c)-6(f) exhibit both metallic and oxidized Ni, Fe,

Cr, and Co on the surfaces of the thin films. Careful comparisons between the metallic and oxide peaks reveal the similar relative peak evolutions for Ni2p, Fe2p, and Co2p rather than Cr2p as a function of the RF powers. Particularly, the oxide peak intensity tends to decrease while the metallic peak intensity tends to increase for Cr2p [see Figs. 6(e)]. In comparison, those of Ni2p, Fe2p, and Co2p do not show such regular evolutions [see Figs. 6(c)-6(d) and 6(f)]. These observations provide a stronger correlation between the evolutions of O and Cr than Ni, Fe, and Co.

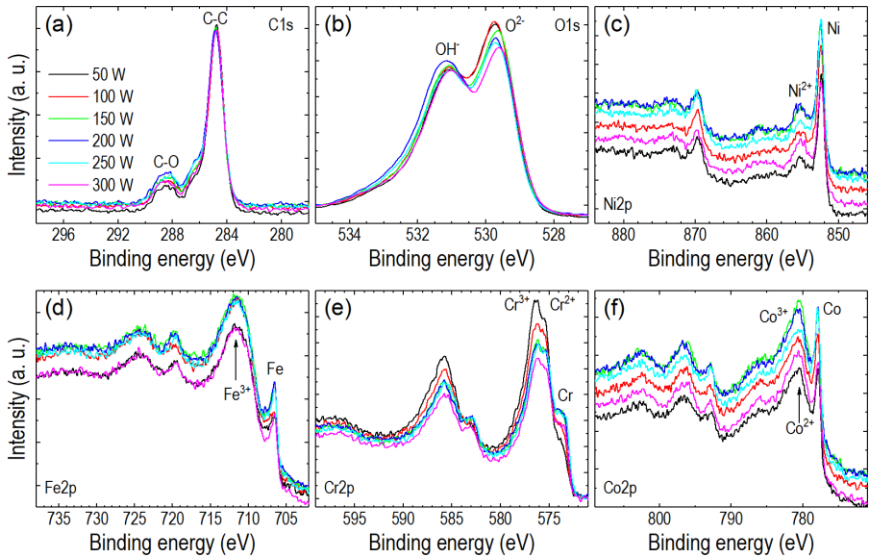

FIG. 6. Core level spectra collected by XPS from the surfaces of the NiFeCrCo HEA thin films deposited by magnetron sputtering with the RF powers at 50-300 W. (a) C1s, (b) O1s, (c) Ni2p, (d) Fe2p, (e) Cr2p, and (f) Co2p.

The atomic compositions derived from the XPS measurements were plotted in Fig. 7(a) as a function of the RF powers. Likewise, those measured by EDX from the surfaces of the same NiFeCrCo HEA thin films were plotted in Fig. 7(b). Since EDX collects the elemental information much deeper than XPS, the comparisons between the elemental compositions probed by XPS and EDX could provide additional information for surface chemistry of the NiFeCrCo HEA thin films, especially atomic segregations of

individual elementals during the magnetron sputtering. In this light, the ratios between the XPS-measured atomic compositions and the EDX-measured atomic compositions for the individual elements are plotted in Fig. 7(c) as a function of the RF powers.

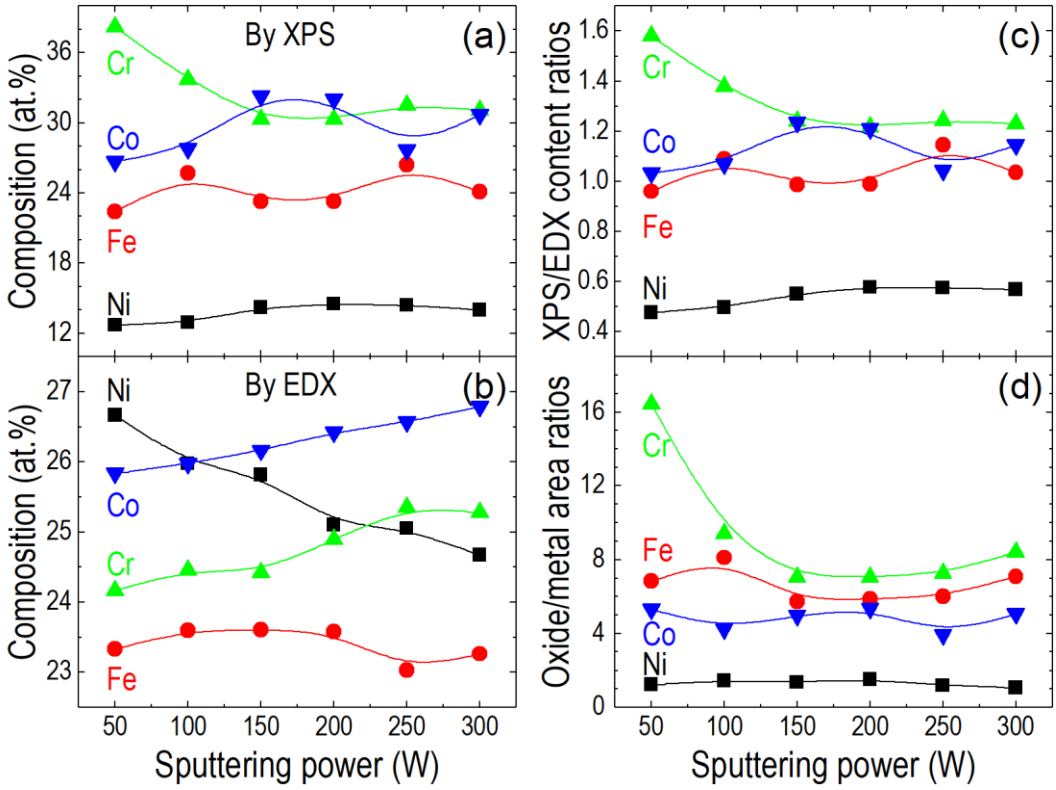

FIG. 7. Relation atomic compositions obtained from the surfaces of the NiFeCrCo HEA thin films by (a) XPS measurements and (b) EDX measurements. (c) Compositional ratios of those measured by XPS over those measured by EDX. (d) XPS peak area ratios of oxide over metal for the individual elements.

Figure 7(c) shows that the XPS/EDX compositional ratios of Cr are larger than 1.0, while those of Ni are smaller than 1.0. In comparison, those of Fe and Co are quite close to each other and around 1.0. These comparisons indicate that Cr tends to segregate onto the growing surface during the magnetron sputtering, and the segregation occurs by interchanging Cr and Ni atoms between the growing surface and its nearest underneath atomic layer, leading to Cr-rich on the surface. Such atomic segregation on the growing

surface along the thin film growth direction is reasonable in terms of the atom size relationship of Cr (0.166 nm) > Fe (0.156 nm) > Co (0.152 nm) > Ni (0.149 nm).[32]

Finally, area ratios between the oxide peaks and metallic peaks were derived from the XPS core level spectra in Figs. 6(c)-6(f) by peak deconvolutions, and the results are presented in Fig. 7(d) as a function of the RF powers. They exhibit oxidation levels of $[Cr]_{Ox}/[Cr]_{Met}$ > $[Fe]_{Ox}/[Fe]_{Met}$ > $[Co]_{Ox}/[Co]_{Met}$ > $[Ni]_{Ox}/[Ni]_{Met}$, which has a strong correlation with those of the XPS/EDX compositional ratios shown in Fig. 7(c). As discussed above, the TEM observations did not resolve the presence of oxide scales within the columnar grain interiors or along the grain boundaries, even in the surface layer [see Figs. 2(c) and 4(c)]. The EDX mappings in Fig. 3 also evidenced that the O-inclusion was due to inward diffusion after deposition rather than in-situ grown during the magnetron-sputtering. In this light, the oxidation levels of $[Cr]_{Ox}/[Cr]_{Met}$ > $[Fe]_{Ox}/[Fe]_{Met}$ > $[Co]_{Ox}/[Co]_{Met}$ > $[Ni]_{Ox}/[Ni]_{Met}$ are attributable to the segregation-induced [Cr] > [Fe] ~ [Co] > [Ni] on the surfaces of the NiFeCrCo HEA thin films. The environmental oxidation in air atmosphere did not cause atomic rearrangement among Ni, Fe, Cr, and Co on the surfaces of the NiFeCrCo HEA thin films, which is different from those observed at elevated temperatures.[33-34]

IV. CONCLUSIONS

The microstructural and surface analyses of the NiFeCrCo-on-Si HEA thin films shows that the RF power during magnetron sputtering strongly influences their growth, defect structures, and surface chemistry. SEM and STEM imaging reveal smooth surfaces below 150 W, while roughening occurs at 150 W and becomes more pronounced at 300

W due to enlarged columnar grains. TEM observations confirmed two types of grain boundaries, i.e., vertical type-I boundaries formed between adjacent columns, and inclined type-II boundaries originating within columns. The inclined boundaries were identified as stacking faults and nanotwins with widths of ~2.0 nm, serving as stress-relief defects and increasing toward the film surface. EDX-STEM mapping shows oxygen enrichment only along type-I boundaries, yet no oxide phases are resolved, indicating that oxygen diffuses inward after deposition rather than forming during sputtering. XPS measurements further reveal mixed metallic and oxidized states for Ni, Fe, Cr, and Co. Comparisons between XPS and EDX compositions indicate that Cr segregates to the growing surface whereas Ni is depleted, consistent with their relative atomic sizes. This segregation explains the oxidation trend of $[Cr]_{Ox}/[Cr]_{Met}$ > $[Fe]_{Ox}/[Fe]_{Met}$ > $[Co]_{Ox}/[Co]_{Met}$ > $[Ni]_{Ox}/[Ni]_{Met}$. The defect formation and Cr-driven segregation collectively govern the microstructural and surface characteristics of the NiFeCrCo HEA thin films.

ACKNOWLEDGMENTS

The authors would like to acknowledge Mr. Roy Lim from Dura- Metal (S) Pte Ltd. for his support in the laser cladding process.

Conflicts of Interest

The authors have no conflicts to disclose.

DATA AVAILABILITY

Data availability on requirement.

REFERENCES

1. Chang, W.-C.; Patel, M. K.; Hsieh, W.-Z.; Chiang, C.-Y.; Ouyang, F.-Y., Synergistic Effect of Nanotwins and Compositional Entropy on the Radiation Resistance of Cocrfeni Thin Films. *Acta Materialia* **2025**, *299*, 121420.

2. Cantor, B.; Chang, I. T. H.; Knight, P.; Vincent, A. J. B., Microstructural Development in Equiatomic Multicomponent Alloys. *Materials Science and Engineering: A* **2004**, *375-377*, 213-218.

3. Yeh, J.-W.; Chen, S.-K.; Lin, S.-J.; Gan, J.-Y.; Chin, T.-S.; Shun, T.-T.; Tsau, C.-H.; Chang, S.-Y., Nanostructured High-Entropy Alloys with Multiple Principal Elements: Novel Alloy Design Concepts and Outcomes. *Advanced Engineering Materials* **2004**, *6*, 299-303.

4. Gong, N., et al., Laser-Cladding of High Entropy Alloy Coatings: An Overview. *Materials Technology* **2023**, *38*, 2151696.

5. Ma, Y.; Peng, G. J.; Wen, D. H.; Zhang, T. H., Nanoindentation Creep Behavior in a Cocrfecuni High-Entropy Alloy Film with Two Different Structure States. *Materials Science and Engineering: A* **2015**, *621*, 111-117.

6. Braeckman, B. R.; Djemia, P.; Tétard, F.; Belliard, L.; Depla, D., Impurity-Controlled Film Growth and Elastic Properties of Cocrcufeni Thin Films. *Surface and Coatings Technology* **2017**, *315*, 475-483.

7. Feng, X. B.; Fu, W.; Zhang, J. Y.; Zhao, J. T.; Li, J.; Wu, K.; Liu, G.; Sun, J., Effects of Nanotwins on the Mechanical Properties of Alxcocrfeni High Entropy Alloy Thin Films. *Scripta Materialia* **2017**, *139*, 71-76.

8. He, F.; Wang, Z.; Wu, Q.; Li, J.; Wang, J.; Liu, C. T., Phase Separation of Metastable Cocrfeni High Entropy Alloy at Intermediate Temperatures. *Scripta Materialia* **2017**, *126*, 15-19.

9. Addab, Y.; Kini, M. K.; Courtois, B.; Savan, A.; Ludwig, A.; Bozzolo, N.; Scheu, C.; Dehm, G.; Chatain, D., Microstructure Evolution and Thermal Stability of Equiatomic Cocrfeni Films on (0001) A-Al2o3. *Acta Materialia* **2020**, *200*, 908-921.

10. Nagy, P.; Rohbeck, N.; Roussely, G.; Sortais, P.; Lábár, J. L.; Gubicza, J.; Michler, J.; Pethö, L., Processing and Characterization of a Multibeam Sputtered

Nanocrystalline Cocrfeni High-Entropy Alloy Film. *Surface and Coatings Technology* **2020**, *386*, 125465.

11. Ustinov, A. I.; Polishchuk, S. S.; Demchenkov, S. A.; Melnychenko, T. V.; Skorodzievskii, V. S., Formation of Thin Foils of High-Entropy Crfeconicu Alloys by Eb-Pvd Process. *Surface and Coatings Technology* **2020**, *403*, 126440.

12. Hu, M.; Cao, Q. P.; Wang, X. D.; Zhang, D. X.; Jiang, J. Z., Tuning Nanostructure and Mechanical Property of Fe–Co–Ni–Cr–Mn High-Entropy Alloy Thin Films by Substrate Temperature. *Materials Today Nano* **2021**, *15*, 100130.

13. Kini, M. K., et al., Nanocrystalline Equiatomic Cocrfeni Alloy Thin Films: Are They Single Phase Fcc? *Surface and Coatings Technology* **2021**, *410*, 126945.

14. Wang, Z.; Wang, C.; Zhao, Y.-L.; Kai, J.-J.; Liu, C.-T.; Hsueh, C.-H., Nanotwinned Cocrfemnni High Entropy Alloy Films for Flexible Electronic Device Applications. *Vacuum* **2021**, *189*, 110249.

15. Gong, N., et al., Synthesis and Structural Characterizations of Crcofenimnx ($0 \leq X \leq 1$) High-Entropy-Alloy Thin Films by Thermal Reduction in Hydrogen. *Journal of Materials Science* **2023**, *58*, 12058-12069.

16. Pristáš, G., et al., Superconductivity in Medium- and High-Entropy Alloy Thin Films: Impact of Thickness and External Pressure. *Physical Review B* **2023**, *107*, 024505.

17. Zhang, M.; Tian, G.; Yan, H.; Guo, R.; Niu, B., Anticorrosive Superhydrophobic High-Entropy Alloy Coating on 3d Iron Foam for Efficient Oil/Water Separation. *Surface and Coatings Technology* **2023**, *468*, 129756.

18. Zhou, R.; Chen, W.; Li, W.; Chou, T.-H.; Chen, Y.-H.; Liang, X.; Luan, J.; Zhu, Y.; Huang, J. C.; Liu, Y., 3d Printed N-Doped Cocrfeni High Entropy Alloy with More Than Doubled Corrosion Resistance in Dilute Sulphuric Acid. *npj Materials Degradation* **2023**, *7*, 8.

19. Cao, Q.; Wang, N.; Kim, J.-M.; Caron, A.; Zhang, Z.; Zhou, H.; Wang, X.; Ding, S.; Zhang, D.; Jiang, J.-Z., A Dual-Phase Fe-Co-Ni-Cr-Mn High Entropy Alloy Thin Film with Superior Strength and Corrosion-Resistance. *Journal of Alloys and Compounds* **2024**, *1003*, 175551.

20. Chen, J.; Liu, X.; Wu, Y.; Linghu, X.; Liu, Y.; Yang, Z.; Cui, D.; He, F., Composition-Dependent Grain Growth Kinetics of Ni-Co-Cr-Fe High-Entropy Alloys. *Applied Physics Letters* **2024**, *125*, 191702.

21. Schwarz, H., et al., Fabrication of Single-Crystalline Cocrfeni Thin Films by Dc Magnetron Sputtering: A Route to Surface Studies of High-Entropy Alloys. *Advanced Materials* **2023**, *35*, 2301526.

22. Wang, J.-J.; Ouyang, F.-Y., Nanotwinned Medium Entropy Alloy Cocrfeni Thin Films with Ultra-High Hardness: Modifying Residual Stress without Scarifying Hardness through Tuning Substrate Bias. *Surface and Coatings Technology* **2022**, *434*, 128191.

23. Kini, M. K.; Lee, S.; Savan, A.; Breitbach, B.; Ghidelli, M.; Ludwig, A.; Scheu, C.; Chatain, D.; Best, J. P.; Dehm, G., Equiatomic Cocrfeni Thin Films on C-Sapphire: The Role of Twins and Orientation Relationships. *Advanced Engineering Materials* **2024**, *26*, 2400720.

24. Zhao, K.; Hao, X.; Huang, B.; Zhao, X.; Ma, J.; Wang, C., Effect of Bias Voltage on the Structure and Properties of Cocrfeni High Entropy Alloy Thin Films Prepared by Magnetron Sputtering. *Materials Today Communications* **2024**, *40*, 110217.

25. Tan, X. Y.; Ng, Y.; Meng, T. L.; Yong, A. M.; Liu, H., Magnetron Sputtering Deposition and Characterization of Nifecrco High Entropy Alloy Thin Films on Rigid and Flexible Substrates. *Surface and Coatings Technology* **2025**, *517*, 132833.

26. Zhang, Z.; Mao, M. M.; Wang, J.; Gludovatz, B.; Zhang, Z.; Mao, S. X.; George, E. P.; Yu, Q.; Ritchie, R. O., Nanoscale Origins of the Damage Tolerance of the High-Entropy Alloy Crmnfeconi. *Nature Communications* **2015**, *6*, 10143.

27. Linder, C.; Boyd, R.; Greczynski, G.; Vagin, M.; Lundin, D.; Törne, K.; Eklund, P.; Björk, E. M., Enhanced Oxygen-Reaction Electrocatalysis and Corrosion Resistance of Cocrfeni Thin Films by Tuned Microstructure and Surface Oxidation. *Small Science* **2024**, *4*, 2400296.

28. Liu, H. F.; Chua, S. J.; Hu, G. X.; Gong, H.; Xiang, N., Annealing Effects on Electrical and Optical Properties of Zno Thin-Film Samples Deposited by Radio Frequency-Magnetron Sputtering on Gaas (001) Substrates. *Journal of Applied Physics* **2007**, *102*, 063507.

29. Liu, H. F.; Chua, S. J.; Hu, G. X.; Gong, H.; Xiang, N., Radio-Frequency Magnetron Sputtering and Wet Thermal Oxidation of Zno Thin Film. *Journal of Applied Physics* **2007**, *102*, 043530.

30. Liu, H. F.; Chua, S. J., Effects of Low-Temperature-Buffer, Rf-Power, and Annealing on Structural and Optical Properties of Zno/Al2o3(0001) Thin Films Grown by Rf-Magnetron Sputtering. *Journal of Applied Physics* **2009**, *106*, 023511.

31. Liu, R.; Wang, C.; Liu, B.; Liu, Y.; Liaw, P. K.; Wang, B., Microstructure and Formation Mechanisms of Nanotwins in the Shear Band in a Feconicrmo0.2 High-Entropy Alloy. *Journal of Materials Research and Technology* **2022**, *20*, 2719-2733.

32. Clementi, E.; Raimondi, D. L.; Reinhardt, W. P., Atomic Screening Constants from Scf Functions. Ii. Atoms with 37 to 86 Electrons. *The Journal of Chemical Physics* **1967**, *47*, 1300-1307.

33. Gong, N., et al., High-Temperature Oxidation and Hot Corrosion of Ni-Based Single Crystal Superalloy in the Incubation Stage. *Corrosion Science* **2023**, *214*, 111026.

34. Liu, H., et al., Hot Corrosion and Internal Spallation of Laser-Cladded Inconel 625 Superalloy Coatings in Molten Sulfate Salts. *Corrosion Science* **2021**, *193*, 109869.